11th World Congress on Computational Mechanics (WCCM XI)
5th European Conference on Computational Mechanics (ECCM V)
6th European Conference on Computational Fluid Dynamics (ECFD VI)
E. Oñate, J. Oliver and A. Huerta (Eds)

A MULTIPLE MARKER LEVEL-SET METHOD FOR SIMULATION OF BUBBLY FLOWS

Néstor Balcázar[1], Lluís Jofre [1], Oriol Lehmkuhl[1,2], Jesús Castro[1], Assensi Oliva[1]

[1] Heat and Mass Transfer Technological Center (CTTC), Universitat Politècnica de Catalunya - BarcelonaTech (UPC), ETSEIAT, Colom 11, 08222 Terrassa (Barcelona), Spain. E-mail: cttc@upc.edu

[2] Termo Fluids, S.L., Avda Jacquard 97 1-E, 08222 Terrassa (Barcelona), Spain. E-mail: termofluids@termofluids.com

Key words: Level-Set Method, Finite-Volume Method, Multiphase Flow, Bubbles, Droplets

Abstract. A multiple marker level-set (MLS) method is introduced for Direct Numerical Simulation of bubbles and droplets, which is integrated in a finite-volume framework on collocated unstructured grids of arbitrary element type. The MLS method is based on the idea of describing separate interfaces in the disperse phase with different level-set functions to prevent numerical and potentially unphysical coalescence of bubbles or droplets without excessive refinement. Thus, bubbles or droplets are able to approach each other closely, within the size of one grid cell, and can even collide, while artificial merging of the interfaces is prevented. The accuracy of the computational method implemented is examined for the problem of a single bubble rising in quiescent liquid. For the validation of the multiple marker level-set method we study the gravity-driven impact of a droplet on a liquid-liquid interface and finally it is applied on simulation of gravity-driven bubbly flow in a vertical pipe.

1 INTRODUCTION

Gravity-driven bubbly flow is a complex phenomenon which is difficult to understand, predict and model. The practical implications of a better understanding and predictive capabilities of this kind of flows is enormous [11]. For instance, in the two-phase bubbly flows in vertical columns, the spatial distribution of the phases controls the pressure drop and the wall heat transfer, therefore its prediction is important for the design of engineering systems. Thus, numerical modelling can help us to shed light on the coupled physical mechanisms of the bubble drift velocity (due to gravity), the turbulence of the liquid phase, the dynamics of the bubbles and the vicinity of a wall. Indeed, the main

emphasis of this work is on the most fundamental level of modelling, namely the Direct Numerical Simulation (DNS) of multiphase flows. In this regard, there are a large choice of interface capturing techniques used in DNS of bubbles and drops, for instance the front tracking (FT) method, the volume-of-fluid (VOF) method, and level-set (LS) methods. A review of advantage and disadvantages of the different techniques used for simulation of multi-fluid flows with sharp interfaces is given in [10]. In this work the conservative level-set (CLS) method introduced by [7] has been selected for interface capturing. Important advantages of CLS method are: mass conservation of fluid phases, a relatively low computational cost, automatic handling of topology changes and efficient parallelization. However, a drawnback of interface tracking methods (VOF, LS and CLS) when they are applied on simulation of bubble swarms is the numerical coalescence of interfaces (see [10]). To overcome this issue, a multiple marker level-set (MLS) method is introduced for simulation of bubbles and drops, which is based on the idea of describing separate interfaces with different level-set functions to prevent numerical and potentially unphysical coalescence of bubbles or droplets without excessive refinement. Thus, bubbles or drops are able to approach each other closely, within the size of one grid cell, and can even collide, while artificial merging of the interfaces is prevented. Therefore, the volume of the bubbles or drops remains constant throughout the simulation. Especially for bubble swarm simulations this is an important aspect (see [11]). As we can infer from previous discussion, the emergence of thin films between interfaces when bubbles or drops collide is a ubiquitous feature in two-phase flow, and the development of an accurate and efficient numerical methodology to simulate this phenomenon without numerical coalescence, using an approach that do not increases the mesh resolution is the main motivation of this work. This paper is organized in the following order: The governing equations employed in this study are given in section 2. Section 3 is devoted to a description of the numerical method, while the simulation results are presented in section 4 Finally, concluding remarks are given in section 5.

2 GOVERNING EQUATIONS

2.1 Incompressible two-phase flow

The Navier-Stokes equations for the dispersed fluid in Ω_d and continuous fluid in Ω_c can be combined into a set of equations in an entire domain $\Omega = \Omega_d \cup \Omega_c$, with a singular source term for the surface tension force at the interface Γ:

$$\frac{\partial}{\partial t}(\rho \mathbf{v}) + \nabla \cdot (\rho \mathbf{v}\mathbf{v}) = -\nabla p + \nabla \cdot \mu \left(\nabla \mathbf{v} + (\nabla \mathbf{v})^T\right) + \rho \mathbf{g} + \mathbf{f}_\sigma \tag{1}$$

where $\mathbf{v}$ and p denote the fluid velocity and pressure field respectively, ρ is the fluid density, μ is the dynamic viscosity, $\mathbf{g}$ is the gravitational acceleration, and $\mathbf{f}_\sigma$ is the surface tension force. Because of incompressibility, the velocity field is divergence-free:

$$\nabla \cdot \mathbf{v} = 0 \tag{2}$$

Physical properties change discontinuously across the interface:

$$\rho = \rho_d H_d + \rho_c(1 - H_d) \qquad (3)$$
$$\mu = \mu_d H_d + \mu_c(1 - H_d)$$

with ρ_d, ρ_c and μ_d, μ_c the densities and viscosities of the disperse and continuous fluids, respectively, and H_d the Heaviside step function that is one in Ω_d and zero elsewhere.

2.2 Multiple marker level-set method

In level-set methods, merging of interfaces happens automatically whenever two interfaces come within one grid cell of each other. To circumvent this issue, we introduce multiple markers ϕ_i (see Eq. 4) to represent each subdomain Ω_i of the disperse phase $\Omega_d = \{\Omega_1, ..., \Omega_{n_d}\}$, where n_d is the number of separate regions included in Ω_d. Thus, the inclusion of separate markers will permit to solve two or more interfaces Γ_i at the same grid cell. Furthermore, in order to limit mass conservation issues, CLS method proposed by [7] is employed for interface capturing. Instead of the signed distance function $d_i(\mathbf{x}, t)$ used to represent the interface in the classical level-set method [9], [7] employed a regularized indicator function, ϕ_i, in the context of their CLS method:

$$\phi_i(\mathbf{x}, t) = \frac{1}{2}\left(tanh\left(\frac{d_i(\mathbf{x}, t)}{2\varepsilon}\right) + 1\right) \qquad \text{with } i = 1, .., n_d \qquad (4)$$

where ε is a tunable parameter that sets the thickness of the profile. With this profile the interface Γ_i is defined by the location of the $\phi_i = 0.5$ iso-surface, $\Gamma_i = \{\mathbf{x} \mid \phi_i(\mathbf{x}, t) = 0.5\}$.

The conservative level-set function ϕ_i is advected by a vector field $\mathbf{v}$ that is, in case of two-phase flows, the solution of the Navier-Stokes equations (Eqs. 1 and 2). The interface transport equation can be written in conservative form provided the velocity field is solenoidal, $\nabla \cdot \mathbf{v} = 0$, namely,

$$\frac{\partial \phi_i}{\partial t} + \nabla \cdot \phi_i \mathbf{v} = 0 \qquad (5)$$

Furthermore, an additional re-initialization equation is introduced to keep the profile and thickness of the interface constant,

$$\frac{\partial \phi_i}{\partial \tau} + \nabla \cdot \phi_i(1 - \phi_i)\mathbf{n}_i|_{\tau=0} = \nabla \cdot \varepsilon \nabla \phi_i \qquad (6)$$

This equation is advanced in pseudo-time τ, it consists of a compressive term, $\phi_i(1 - \phi_i)\mathbf{n}_i|_{\tau=0}$, wich forces the level-set function to be compressed onto the interface along the normal vector $\mathbf{n}_i$, and of a diffusion term $\nabla \cdot \varepsilon \nabla \phi_i$ that ensure the profile remains of characteristic thickness ε. Geometrical information on the interface Γ_i, such as normal vector $\mathbf{n}_i$ or curvature κ_i, is obtained through:

$$\mathbf{n}_i(\phi_i) = \frac{\nabla \phi_i}{\|\nabla \phi_i\|} \qquad (7)$$

$$\kappa_i(\phi_i) = -\nabla \cdot \mathbf{n}_i \tag{8}$$

The accurate computation of the surface tension ($\mathbf{f}_\sigma$ in Eq. 1) is one of the most critical elements of any method designed to follow the motion of the interface between immiscible fluids. Implementing surface tension in a numerical scheme involves two issues: the curvature κ_i needs to be determined, and the resulting pressure jump must be applied appropriately to the fluids. Because finite-volume method will be used for discretization of governing equations, the aforementioned problems can be conveniently addressed through the continuous surface force (CSF) method [3], which has been extended to include multiple markers in the same grid cell. Thus, the singular term, $\mathbf{f}_\sigma$ in Eq. 1, is converted to a volume force as follows,

$$\mathbf{f}_\sigma = \sigma \sum_i \kappa_i(\phi_i) \nabla \phi_i \tag{9}$$

where κ_i is given by Eq. (8) and σ is the surface tension coefficient. In addition, the fluid properties are regularized by employing a global level-set function ϕ_d for the disperse phase,

$$\rho = \rho_d \phi_d + \rho_c(1 - \phi_d) \qquad \mu = \mu_d \phi_d + \mu_c(1 - \phi_d) \tag{10}$$

where,

$$\phi_d(\mathbf{x}, t) = max\{\phi_1(\mathbf{x}, t), ..., \phi_{n_d-1}(\mathbf{x}, t), \phi_{n_d}(\mathbf{x}, t)\} \tag{11}$$

3 NUMERICAL METHOD

The governing equations have been discretized on a collocated unstructured grid arrangement by means of the finite-volume method, hence, all computed variables are stored at cell centroids. In order to avoid unphysical oscillations in the level-set function, a TVD Superbee limiter, is used to discretize the convective term in advection Eq. (5). Central difference scheme, is used to discretize both the convective and compressive terms of momemtum Eq. (1) and re-initialization Eq. (6), respectively. A distance-weighted linear interpolation is used to find the face values of physical properties and interface normals, while gradients are computed at cell centroids by using the least-squares method.

The velocity-pressure coupling has been solved by means of a classical fractional step projection method. Momentum Eq. (1) is decomposed into two steps:

$$\frac{\rho \mathbf{v}^* - \rho \mathbf{v}^n}{\Delta t} = -\frac{3}{2}\mathbf{A}_h(\rho \mathbf{v}^n) + \frac{1}{2}\mathbf{A}_h(\rho \mathbf{v}^{n-1}) + \mathbf{D}_h(\mathbf{v}^n) + \rho \mathbf{g} + \sigma \sum_i \kappa_i \nabla_h(\phi_i) \tag{12}$$

and

$$\mathbf{v}^{n+1} = \mathbf{v}^* - \frac{\Delta t}{\rho} \nabla_h(p^{n+1}) \tag{13}$$

where ∇_h represents the gradient operator, $D_h(\mathbf{v}) = \nabla_h \cdot \mu \left(\nabla_h \mathbf{v} + \nabla_h^T \mathbf{v} \right)$ represents the diffusion operator, and $\mathbf{A}_h(\rho \mathbf{v}) = \nabla_h \cdot (\rho \mathbf{v} \mathbf{v})$ is the advection operator. The resulting velocity $\mathbf{v}^*$ from Eq. (12), which does not satisfy the continuity Eq. (2), is corrected by

Eq. (13). Substituting Eq. (12) into the continuity Eq. (2) yields a Poisson equation for pressure,

$$\nabla_h \cdot \left(\frac{1}{\rho} \nabla_h (p^{n+1}) \right) = \frac{1}{\Delta t} \nabla_h \cdot (\mathbf{v}^*) \tag{14}$$

Poisson Eq. (14) discretization, leads to a linear system; the system matrix is symmetric and positive definite. We have developed a preconditioned conjugate gradient method in our code, wich is used to solve Eq. (14). In order to avoid pressure-velocity decoupling when the pressure projection is made on collocated meshes [8], a cell face velocity $\mathbf{v}_f$ is defined so that $\nabla_h \cdot \mathbf{v} = 0$ (see Eq. 2) in each control volume. Namely in discretized form:

$$\mathbf{v}_f = \sum_{q \in \{P,F\}} \frac{1}{2} \left(\mathbf{v}_q^{n+1} + \frac{\Delta t}{\rho(\phi_q^n)} (\nabla_h p^{n+1})_q \right) - \frac{\Delta t}{\rho_f} (\nabla_h p^{n+1})_f \tag{15}$$

where P and F are denoting the adjacent cell nodes to the face f. This velocity is used to advect the markers and momentum in Eq. 5 and Eq. 12 respectively. For the temporal discretization, explicit Adams-Bashforth scheme is used for the momemtum Eq. (12), while for the corrector Eq. (13) an explicit first-order scheme has been used. Advection Eq. (5) and re-initialization Eq. (6) are integrated in time with a 3-step third-order accurate TVD Runge-Kutta method. Solving Eq. (6) to steady-state results in a smooth transition of ϕ at the interface that depends of the diffusion coefficient ε. In this paper, all numerical simulations were performed by setting $\varepsilon = 0.5h$ where $h = (V_{cell})^{1/3}$ is the characteristic size of the grid cell. Therefore, ε is chosen to be as small as possible in order to limit mass conservation errors, while maintaining reasonable resolution of the conservative level-set function to avoid numerical issues. In our simulations two or three iterations per physical time step of re-initialization Eq. (6) are sufficient to keep the profile of the level-set function. Thus, our computational approach for simulation of bubbles and drops without numerical coalescence can be summarized as follows:

1. Initialization of $\mathbf{v}_P$ ($P \equiv$ cell centroid), $\mathbf{v}_f$ ($f \equiv$ face centroid), and ϕ_i for $i = 1, .., n_d$.
2. Advection (using $\mathbf{v}_f$) and re-initialization of ϕ_i for $i = 1, .., n_d$
3. Computation of $\mathbf{n}_i$, κ_i for $i = 1, .., n_d$, and ϕ_d, ρ_d, μ_d
4. Computation of $\mathbf{v}_P$ and p by solving Eq. 12, Eq. 14 and Eq. 13.
5. Computation of $\mathbf{v}_f$ by Eq. 15.
6. Repeat steps 2-5 until time step required.

The described numerical methods were implemented in an in-house solver called TermoFluids, wich is a code designed for Direct Numerical Simulation and Large Eddy Simulation of turbulent flows. The reader is referred to [5] for details on the TermoFluids framework that are beyond the scope of this paper.

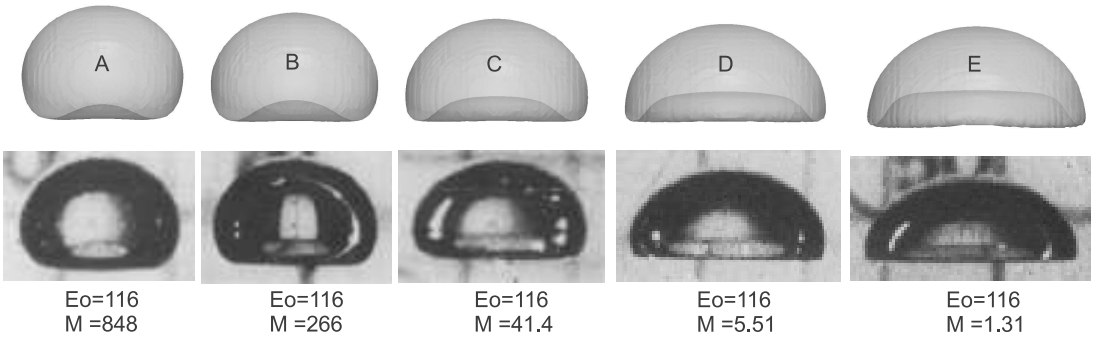

Figure 1: Comparison of numerical results (top) against experiments from [2] (bottom), each case has been identified with capital letters.

Case	Eo	M	Re_{exp}	Re_{num}	ϵ_r
A	116	848	2.47	2.29	7.29%
B	116	266	3.57	3.54	0.80%
C	116	41.4	7.16	6.94	3.03%
D	116	5.51	13.3	12.86	3.38%
E	116	1.31	20.4	19.38	5.00%

Table 1: Comparison of numerical results (Re_{num}) with experiments (Re_{exp}) from Bhaga et al. [2]. Here, $\epsilon_r = 100 \cdot Re_{exp}^{-1} |Re_{exp} - Re_{num}|$

4 RESULTS AND DISCUSSION

4.1 Rising bubble

Preliminary computations were performed in order to test the accuracy of the implemented numerical methods. The experiments of [2] and others provide a fairly detailed picture of the motion of bubbles and droplets through a quiescent viscous liquid. The relevant physical quantities in their experiments can be summarized in the next parameters:

$$M \equiv \frac{g\mu_c^4 \Delta\rho}{\rho_c^2 \sigma^3} \qquad Eo \equiv \frac{gd^2\Delta\rho}{\sigma} \qquad Re \equiv \frac{\rho_c U_T d}{\mu_l} \qquad \eta_\rho \equiv \frac{\rho_c}{\rho_d} \qquad \eta_\mu \equiv \frac{\mu_c}{\mu_d} \tag{16}$$

where, η_ρ and η_μ are respectively the density and viscosity ratio; M is the Morton number, $\Delta\rho = \rho_c - \rho_d$, specifies the density difference between the fluid phases; Eo is the Eötvös number, Re is the Reynolds number and U_T is the vertical velocity of the bubble. All numerical experiments were performed on a cylindrical domain with diameter $D_\Omega = 8d$ and height $H_\Omega = 8d$, where d is the spherical volume equivalent diameter of the bubble. Periodic boundary conditions were applied at the top and bottom boundaries, and Neumann boundary condition at the side wall. For gravity-driven bubbly flows in periodic domains, it is necesary to ensure that the net resultant force in the direction of gravity is zero. Hence, a force equal to the space-averaged density times the gravitational

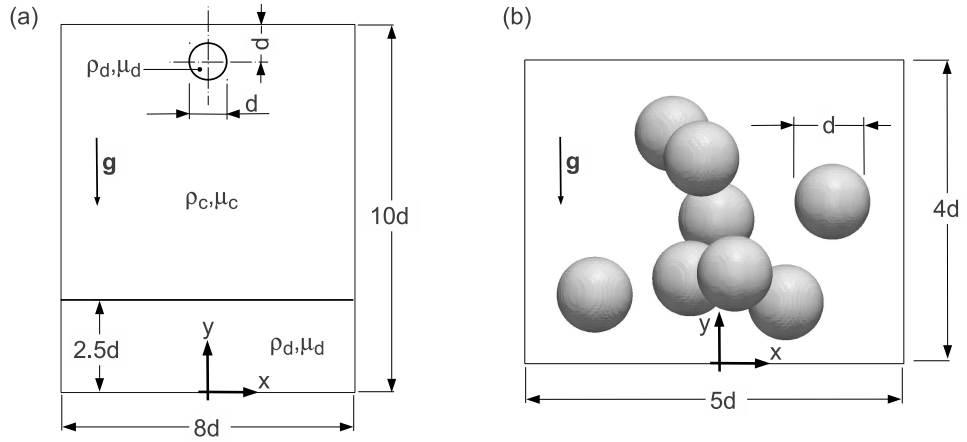

Figure 2: Computational set-up and initial condition for (**a**) Drop impact on a liquid-liquid interface and (**b**) Free bubble array used as initial condition for gravity-driven bubbly flow in a vertical pipe

acceleration, $\rho_0 \mathbf{g}$ where $\rho_0 = \int_\Omega (\phi_d \rho_d + (1-\phi_d)\rho_c)\, dV$, is subtracted from the right hand side of Eq. 1. The computational domain was discretized with 1.5×10^6 hexahedral control volumes, which is equivalent to 30 CV/d (control volumes per bubble diameter). All numerical experiments were performed setting $Eo = 116$, $\eta_\rho = 100$, $\eta_\mu = 100$ and $1.0 < M < 10^3$. Fig. 1 compares numerical results with previous experiments reported by [2]. The final bubble shape is given by the relative strength of the flow forces and the surface tension force, which are given by Re and Eo, respectively. Indeed, numerical predictions and experimental findings of [2] are in close agreement, as shown in Fig. 1 and Table 1.

4.2 Drop impact on a liquid-liquid interface

In this section, the gravity-driven impact of a single drop onto a liquid-liquid interface is studied in order to validate the accuracy of the MLS method against experimental and numerical data reported by [6] y [4] respectively. Numerical simulations were performed for a set of parameters corresponding to conditions of experiments in [6]: $Eo = 6.4$, $M = 8.822 \times 10^{-8}$, $\eta_\rho = 1.189$ and $\eta_\mu = 0.332$, namely, water as dispersed phase and silicon oil as continuous phase. For the sake of comparison, we also introduce the following non-dimensional time, $t^* = t/t_i$, where $t_i = d/U_i$ and U_i is equivalent to the drop terminal velocity. The computational set-up is schematically indicated in Fig. 2a. The size of the cylindrical domain is fixed to $D_\Omega \times H_\Omega = 8d \times 10d$, where d is the initial diameter of the spherical drop. Thus, confinement effect is minimized, while the droplet has enough approach distance to reach terminal velocity before impact. No-slip boundary conditions are imposed at the top ($y = H_\Omega$) and bottom ($y = 0$) walls, and free-slip boundary condition is used at the lateral boundary ($r = 0.5 D_\Omega$). Fig. 2b shows the mesh used in numerical simulations. The domain was divided in 6×10^6 hexahedral control volumes.

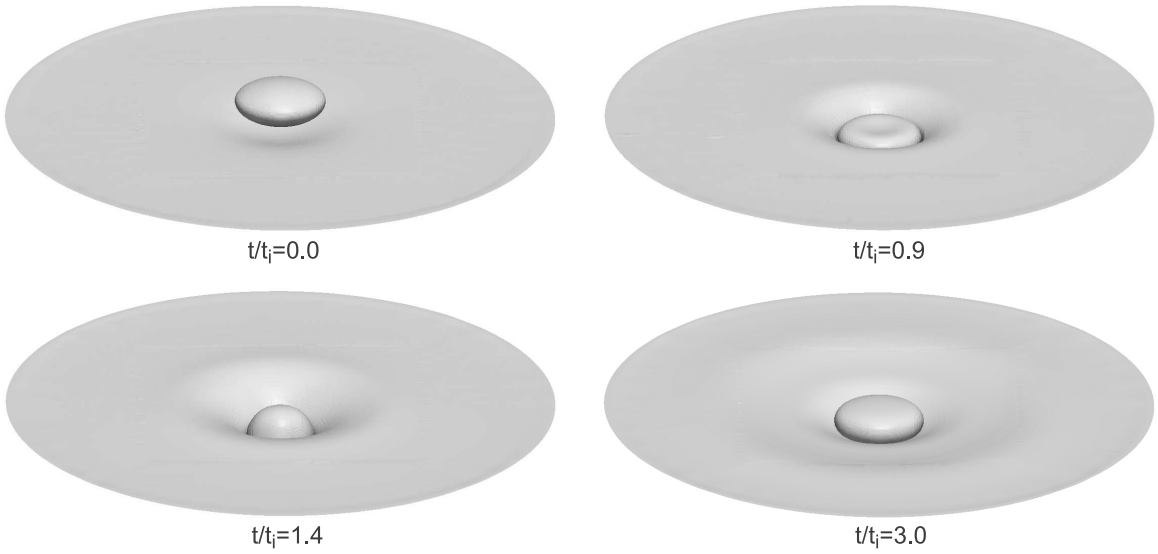

Figure 3: Snapshots of the drop impact onto a liquid-liquid interface, $Eo = 6.4$, $M = 8.822 \times 10^{-8}$, $\eta_\rho = 1.189$ and $\eta_\mu = 0.332$.

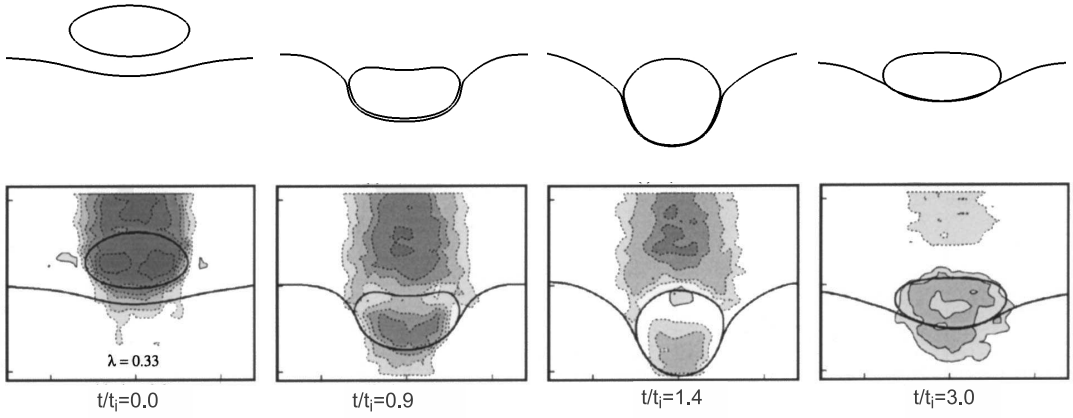

Figure 4: Comparison of numerical results (top) against experiments reported by [6] (bottom).

Fig. 3 shows the time evolution of the drop collision. Prior to the impact, the approach is nearly linear in time (see Fig. 5) until the collision between the drop and liquid-liquid interface is achieved. Before the collision, the droplet decelerates and the trapped fluid near the free surface is drained radially outward, while the gap between the drop and the interface is reduced until a thin fluid layer remains. Indeed, coalescence is inhibited by the

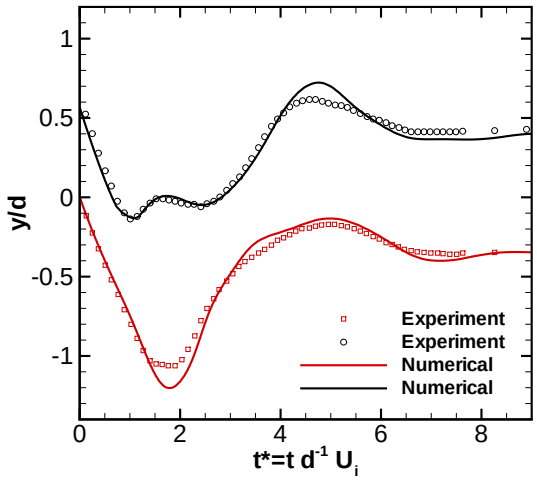

Figure 5: Comparison of numerical (lines) and experimental (symbols) results for the normalized locations of the interface, lower drop surface (dashdot, squares), and upper drop surface (dashed, line) on the centerline relative to the quiescent liquidliquid interface.

thin film of continuous fluid trapped between the drop and the interface. In experiments reported by [6] a direct analysis of the flow images showed that the film thickness is of order $400\mu m$ when the macroscopic steady state is achieved. After collision, oscillations were observed on the interfaces. The drop then streches horizontally as it touches the interface. With time, the remaining inertia inside the drop deflects the interface to a maximun while the drop extends vertically at the same time. The interface continue to deform until they reach a steady state approximately $7t_i$ after impact. In Fig. 4, a comparison of the numerical and experimental drop/interface topologies at time $t/t_i = \{0.0, 0.9, 1.4, 3.0\}$ are shown. The agreement between the simulation and experiment is excellent. In Fig. 5, the normalized locations z/d of the numerical upper and lower drop surfaces are shown as a function of dimensionless time t/t_i. Numerical results are very close to experimental data reported by [6], as shown in Fig. 4 and Fig. 5. Similar results were reported also by [4].

4.3 Gravity-driven bubbly flow in a vertical pipe

With the confidence that MLS method has been validated in previous section, a numerical experiment is carried out to predict the gravity-driven bubbly flow in a vertical pipe. The computational set-up is specified as a circular channel bounded by a rigid wall (see Fig. 2b). The size of the domain is $D_\Omega \times H_\Omega = 5d \times 4d$, which has been discretized by 1.2×10^6 hexahedral volumes. Thus, the equivalent bubble diameter, d, is resolved by 25 mesh cells. Imposed boundary conditions are non-slip at the rigid wall and periodic on the streamwise (y-direction). In this way bubbles go out of the domain on the top

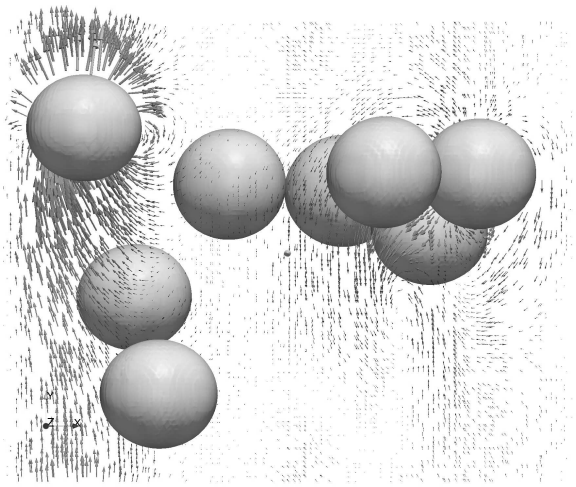

Figure 6: The 8 bubbles with $Eo = 0.5$, $M = 1 \times 10^{-8}$,$\eta_\rho = 10$,$\eta_\mu = 10$ at time $t^* = 15$. Velocity vectors in a plane cross-section is shown at $z = 0$.

side, and they come back in the domain again from the opposite side. A free bubble array of 8 bubbles are initially placed following a random pattern. This corresponds to a dilute bubbly flow, with an overall volumetric fraction of $\alpha = 2.7\%$. Since both fluids are assumed to be incompressible , α is constant throughout the simulation. We do not allow coalescence of bubbles, so that statistics can be obtained for a constant number of bubbles. Physical parameters are fixed to $Eo = 0.5$, $M = 1 \times 10^{-8}$, $\eta_\rho = 10$ and $\eta_\mu = 10$, which corresponds to nearly spherical bubbles. As initial condition, both bubbles and liquid are quiescent. Individual bubble trajectories are presented at Fig. 7b. It can be seen that the bubbles move, not only in streamwise direction, both also in radial direction. These radial movements of bubbles tend to align bubbles at aproximately constant distance from the wall making a bubble curtain between the symmetric axis of the domain and a downward fluid liquid layer next to the wall (see Fig. 7c and Fig. 7d). Even though the individual bubble motion show a transient behaviour due the wake interaction, the whole swarm of bubbles reaches a steady state at approximately $t^* = 15$ (see Fig. 7a). Bubbles also tend to align themselves horizontally, phenomenon which is known as the bubble rafting [1]. When all bubbles are at approximately the same vertical position, the probability of collision increases. A collision of a bubble with the wall was observed at $t^* = 33$. At this instant, simulation was stopped, because especial treatment for interaction between bubble and wall has not been considered in the current work.

5 CONCLUSIONS

In this paper we have presented a multiple marker level-set method for simulation of bubbles and drops without numerical merging of interfaces. The numerical method has been applied on simulation of the drop impact on a liquid-liquid interface, and gravity-

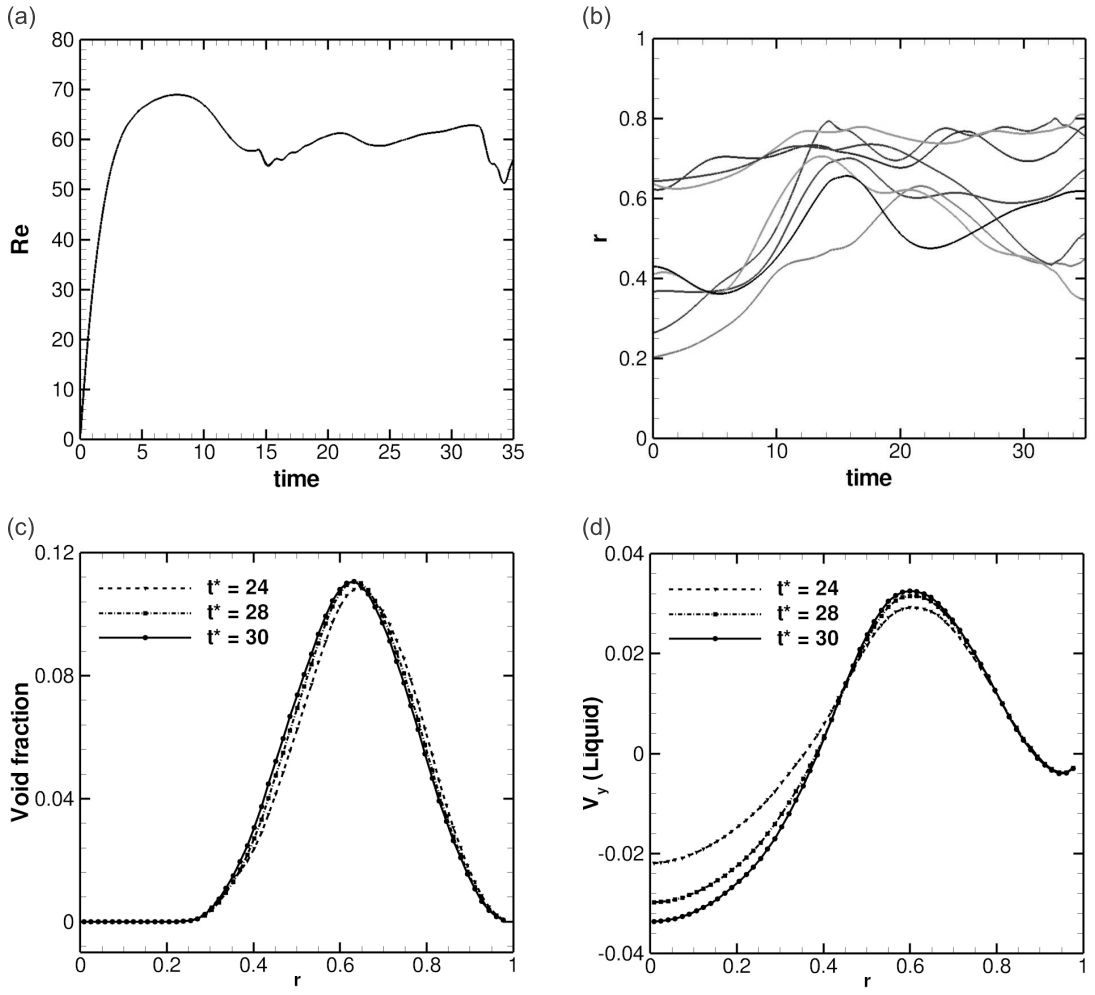

Figure 7: (**a**) Time evolution of Reynols number, $Re = \frac{\rho_d d U_y}{\mu_d}$, with $U_y = \int_\Omega \phi_d v_y dV$ (**b**) Radial trajectories of the bubbles. (**c**) Average void fraction of the bubbles from $t^* = 15$. (**d**) Average liquid velocity from $t^* = 15$

driven bubbly flow in a vertical column. Numerical results are in close agreement with experiments, and they show that multiple marker level-set method is a suitable tool for simulation of bubble swarms.

6 Acknowledgments

This work has been financially supported by the Ministerio de Economía y Competitividad, Secretaría de Estado de Investigación, Desarrollo e Innovación, Spain (ENE2011-28699), and by Termo Fluids S.L.

REFERENCES

[1] Bunner, B., Tryggvason, G., Effect of bubble deformation on the properties of bubbly flows, *J. Fluid Mech.*, Vol. **495**, 77–118, 2003.

[2] Bhaga, D., Weber, M.E., Bubbles in viscous liquids: shapes, wakes and velocities, *J. Fluid. Mech.*, Vol. **105**, 61–85, 1981.

[3] Brackbill, J.U., Kothe, D.B., Zemach, C., A Continuum Method for Modeling Surface Tension, *J. Comput. Phys.* Vol. **100**, 335–354. 1992.

[4] Coyajee, E., Boersna, J.B., Numerical simulation of drop impact on a liquid-liquid interface with a multiple marker front-capturing method, *J. Comp. Phys.*, Vol. **228**, 4444–4467, 2009.

[5] Lehmkuhl, O., Perez-Segarra, C.D., Soria, M., Oliva, A., A new Parallel unstructured CFD code for the simulation of turbulent industrial problems on low cost PC cluster, Proceedings of the Parallel CFD 2007 Conference, 1–8, 2007.

[6] Mohamed-Kassim, Z., Longmire, E.K., Drop impact on a liquid-liquid interface, *Phys. Fluids*, Vol. **15**, 3263–3273, 2003.

[7] Olsson, E., Kreiss, G., A conservative level set method for two phase flow, *J. Comp. Phys.*, Vol. **210**, 225-246, 2005.

[8] Rhie, C.M., Chow, W.L., Numerical Study of the Turbulent Flow past an Airfoil with Trailing Edge Separation, *AIAA J.*, Vol. **21**, 1525–1532, 1983.

[9] Sussman, M., Fatemi, E., Smereka, P., An Improved Level Set Method for Incompressible Two-Phase Flows, *Journal of Computers and Fluids*, Vol. **27** 663–680, 1998.

[10] Van Sint Annaland, M., Deen, N.G., Kuipers, J.A.M., Numerical Simulation of gas bubbles behaviour using a three-dimensional volume-of-fluid method, *Chemical Engineering Science*, Vol. **60**, 2999–3011, 2005.

[11] Tryggvason, G., Dabiri, S., Abouhasanzadeh, B., Jaicai, L., Multiscale considerations in direct numerical simulations of multiphase flows, *Phys. Fluids*, Vol. **25**, 031302, 2013.